Acta Pharmaceutica Sinica B 2026;16(5):3211−3223

Chinese Pharmaceutical Association
Institute of Materia Medica, Chinese Academy of Medical Sciences

Acta Pharmaceutica Sinica B

www.elsevier.com/locate/apsb
www.sciencedirect.com

ORIGINAL ARTICLE

Multistage responsive microneedle delivery system loaded oncolytic virus for topical therapy of melanoma

Zhongjie Wang[a], Zewei Yan[c], Hanlin Chen[a], Yue Wang[b], Yingjie Shi[b], Yuantian Jing[a], Ruiqi Ming[a], Shujun Liu[a], Pengfei Jin[b,*], Guanghao Wu[a,*], Lili Huang[a,*]

[a]*School of Medical Technology, Beijing Institute of Technology, Beijing 100081, China*
[b]*Department of Pharmacy, Beijing Hospital, National Center of Gerontology, Institute of Geriatric Medicine, Chinese Academy of Medical Sciences, Beijing Key Laboratory of Assessment of Clinical Drugs Risk and Individual Application, Beijing 100730, China*
[c]*School of Life Sciences, Inner Mongolia Normal University, Hohhot 010022, China*

Received 2 July 2025; received in revised form 4 September 2025; accepted 30 September 2025

KEY WORDS

Multistage microneedle;
Oncolytic viruses;
Melanoma;
Tumor microenvironment;
JQ1;
PD-L1;
Lactate metabolism;
Immune synergism

Abstract Melanoma, the most aggressive form of skin cancer, remains a formidable therapeutic challenge. While oncolytic viruses (OVs) exhibit promising antitumor potential, their efficacy is often limited by insufficient intratumoral viral replication, poor tissue penetration, and the immunosuppressive tumor microenvironment (TME). Herein, a multistage microneedle (MN-OJ) system designed to amplify both local oncolysis and systemic antitumor immunity mediated by oncolytic adenovirus (OA) in melanoma. The dissolvable MN base facilitates rapid OA delivery, inducing tumor cell lysis and subsequent release of tumor-associated antigens to prime T-cell responses. Concurrently, the degradable MN tip enables sustained release of JQ1, which enhances OA replication, modulates lactic acid levels and PD-L1 expression, thereby reprogramming the immunosuppressive TME to promote T-cell infiltration and cytotoxicity. In murine models, MN-OJ demonstrated potent inhibition of both primary and distal tumors, without systemic toxicity. This innovative platform combines immediate tumor destruction with sustained immune modulation, offering a promising clinical approach for melanoma therapy.

*Corresponding authors.
E-mail addresses: llhuang@bit.edu.cn (Lili Huang), j790101@163.com (Pengfei Jin), gwu@bit.edu.cn (Guanghao Wu).

Peer review under the responsibility of Chinese Pharmaceutical Association and Institute of Materia Medica, Chinese Academy of Medical Sciences.

https://doi.org/10.1016/j.apsb.2026.02.015

1. Introduction

Melanoma, the most aggressive form of skin cancer, exhibits high metastatic potential and mortality rates[1,2]. While early-stage lesions are often curable by resection, recurrence occurs in ∼40% of cases[3], and metastatic disease reduces 5-year survival to just 27%[4−6]. Current treatments, including chemotherapy, radiotherapy, and immune checkpoint blockade[7−9], are limited by suboptimal efficacy and systemic toxicity[10−12]. There exists an urgent clinical need to develop novel therapeutic strategies with superior efficacy, enhanced selectivity, and reduced toxicity that can effectively manage both primary and recurrent melanomas, thereby improving patient survival and quality of life.

Oncolytic virus (OVs), particularly oncolytic adenovirus (OA), offers a promising alternative owing to its tumor-selective replication, mild side effects, and low risk of resistance[13−15]. Moreover, it has been demonstrated to elicit a dual therapeutic effect by selectively infecting and lysing tumor cells *in situ*, while simultaneously stimulating systemic antitumor immunity to suppress recurrence and metastasis[16−18]. Nevertheless, clinical trials reveal that OA monotherapy has not substantially improved overall survival[19−21]. The key limitations include the abnormal metabolism of tumor cells that impairs viral proliferation, and the dense extracellular matrix (ECM) within tumors that impedes viral dissemination, both of which reduce cytotoxic efficacy[22,23]. Additionally, the immunosuppressive tumor microenvironment (TME) presents additional challenges, including PD-L1 overexpression, accumulation of lactic acid, and elevated anti-inflammatory cytokines[24−26]. These features not only compromise OA-mediated immune activation but also actively promote tumor progression and metastasis. Therefore, further enhancing both local oncolysis and systemic antitumor immunity is highly desirable for OA-based antitumor therapy.

JQ1, currently under clinical investigation as a novel antitumor agent, has demonstrated promising efficacy and safety across a range of cancer types[27−29]. Its primary antitumor mechanism involves the specific inhibition of the bromodomain and extra-terminal (BET) protein family's binding to chromatin, which effectively suppresses gene transcription associated with cancer progression[30,31]. Moreover, JQ1 can produce synergistic effects when combined with other therapeutic modalities[32,33]. Emerging research indicates that JQ1 also potentiates the antitumor immune response of T cells through multiple pathways. This includes modulating the tumor microenvironment to facilitate T cell activation and infiltration, as well as inhibiting PD-L1 expression on tumor cells, which in turn amplifies the recognition and cytotoxicity of effector T cells against tumor cells[34,35]. These findings highlight its promising role in cancer immunotherapy.

In this study, we developed an innovative multistage microneedle (MN) patch for sequential delivery of OA and the small-molecule modulator JQ1 (Scheme 1A). The water-soluble hyaluronic acid (HA) base for OA loading and rapid release, poly(lactic-*co*-glycolic acid) (PLGA) needle tips ensuring controlled JQ1 delivery. Upon dermal insertion, the MNs create microchannels that enable direct OA delivery across the stratum corneum into tumor tissue, ensuring widespread distribution. The rapidly released OA effectively lyses tumor cells and stimulates the immune response through triggering the release of tumor-associated antigens (TAAs) and damage-associated molecular patterns (DAMPs). Simultaneously, sustained JQ1 release enhances OA replication through viral early gene upregulation and remodel the TME *via* coordinated lactate depletion and PD-L1 downregulation. This dual action robustly activates CTLs, as shown by increased T-cell effector function and tumor cell clearance (Scheme 1B). The combined oncolytic and immunomodulatory effects mediate durable antitumor responses following single-dose treatment.

2. Materials and methods

2.1. Materials and reagents

DMEM, RPMI-1640 cell culture medium, fetal bovine serum (FBS) and 0.25% trypsin-ethylenediaminetetraacetic acid (EDTA) were purchased from Gibco (Grand Island, NY, USA). Penicillin−streptomycin was purchased from Macgene (Beijing, China). HA (catalogue no. H909935) was purchased from Macklin (Shanghai, China). PLGA (catalogue no. 719897) was purchased from Sigma−Aldrich (St. Louis, MO, USA). FITC (catalogue no. 2284MG050) was purchased from Biofroxx. RB (catalogue no. R104960) was purchased from Aladdin (Shanghai, China). Anti-CDK9 antibody (catalogue no. K006698P), anti-β-actin (catalogue no. K200058M), anti-c-Myc antibody (catalogue no. K007442P), anti-LDHA antibody (catalogue no. K007244P), anti-HK-2 antibody (catalogue no. K001797P), anti-BRD4 antibody (catalogue no. K009002P) were purchased from Solarbio (Beijing, China). Goat-anti-rabbit IgG (HRP) (catalogue no. ab6721) antibodies was purchased from Abcam (Cambridge, MA, USA). APC-conjugated anti-mouse CD274 (catalogue no. 124311), APC-conjugated anti-mouse CD11c (catalogue no. 117310) antibody, FITC-conjugated anti-mouse CD80 (catalogue no. 104705), PE-conjugated anti-mouse CD86 (catalogue no. 159203), APC-conjugated anti-mouse CD3 (catalogue no. 100312), FITC-conjugated anti-mouse CD8 (catalogue no. 100705), PE-conjugated anti-mouse IFN-γ (catalogue no. 505807), PE-conjugated anti-mouse CD44 (catalogue no. 103007), Pacific Blue-conjugated anti-mouse CD62L antibody (catalogue no. 104424) were purchased from BioLegend (San Diego, CA,USA). Micro BCA Protein Assay Kit and Prestained Protein Ladder were purchased from Thermo Scientific (Waltham, MA, USA). Coomassie brilliant blue, Cell Counting Kit-8 (CCK-8), Silver stain kit and SDS-PAGE loading buffer were purchased from Solarbio (Beijing China). Hoechst 33342 was purchased from Life Technologies (Gaithersburg, MD, USA). Recombinant murine IL-4 and granulocyte-macrophage colony

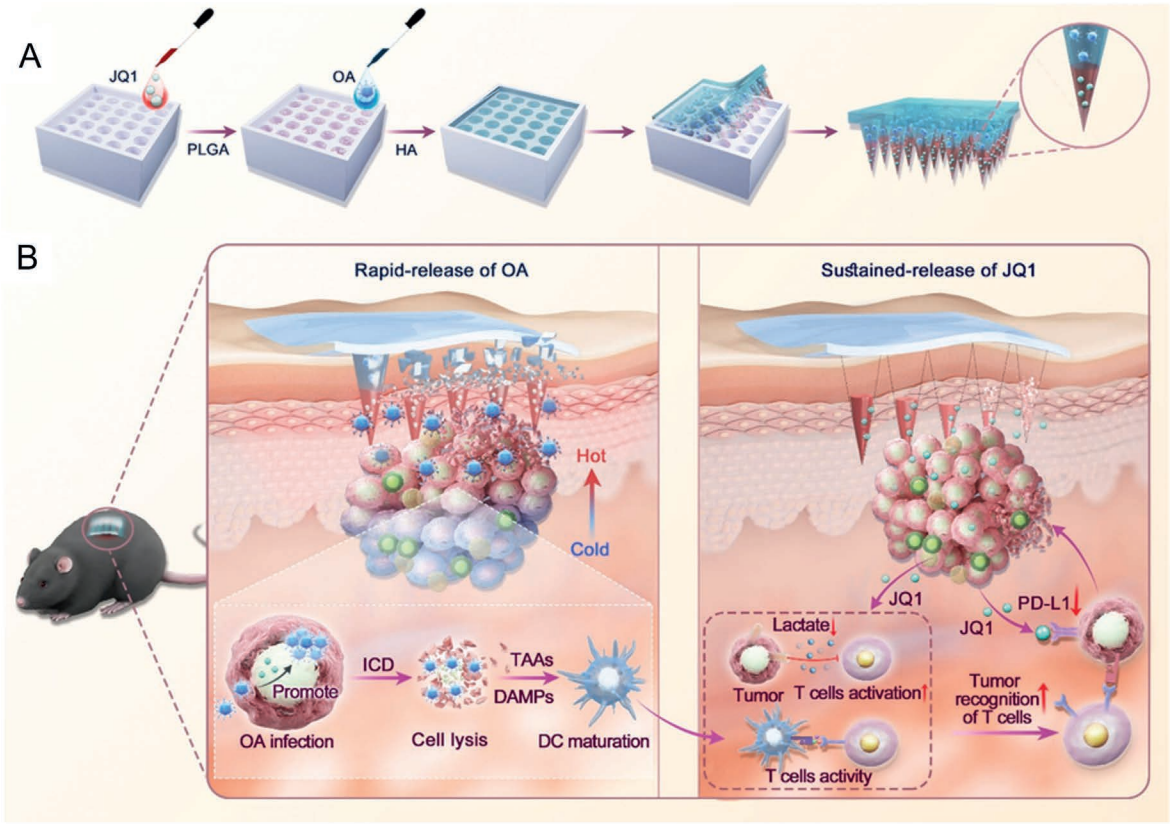

Scheme 1 Schematic illustration of multistage MN-OJ patch for melanoma therapy. (A) The construction of multistage MN-OJ patch. (B) The synergistic antitumor mechanism of multistage MN-OJ patch.

stimulating factor (GM-CSF) were purchased from PeproTech (Rocky Hill, NJ, USA).

2.2. *Preparation of MN-OJ patch*

To prepare the MN-OJ patch, two solutions were sequentially cast onto the mold. 0.1 g of PLGA was dissolved in 2 mL of 1,4-dioxane to obtain a 5% (*w*/*v*) PLGA solution, 100 mg of JQ1 was dissolved in the 5% (*w*/*v*) PLGA solution to obtain the first casting solution (JQ1/PLGA). Add the obtained mixture to the PDMS mold, and place it in a vacuum drying oven for a continuous vacuum pumping and degassing process 3 times, 5 min each time. After removing the excess solution from the surface of the mold, dry the sample in an oven at 37 °C overnight. Next, a 10% (*w*/*v*) HA hydrogel solution was prepared by dissolving 50 mg of HA in 5 mL of PBS, followed by the addition of OA. The mixture was stirred for 1 h to obtain OA/HA solution. Add the second casting solution to the surface of the dried PDMS mold and perform vacuum treatment as described above. Dry the mold in a 37 °C oven overnight, replenishing the HA gel three times during this period. Finally, gently peel off the patch from the mold to obtain the PLGA&HA MN patch.

2.3. *Skin penetration test*

To prove that microneedles have the potential to penetrate the skin, the skin samples were obtained from 6-week old mice and then cleaned with alcohol wipes after using depilatory cream to remove excess hair from the mice. The FITC- and RB-loaded MN patches were pressed onto these tissues for 10 min to dissolve the base and detach the needles, after which the base was removed and the skin tissue was stained with methylene blue for 10 min before wiping away any remaining dye on the surface and the skin samples were observed under an optical microscope. Then prepare tissue sections, stain them with H&E, and observe them through a slide scanner (Olympus, VS200, Tokyo, Japan).

2.4. *In vitro drug release*

The FITC- and RB-loaded MN patches were immersed in 2 mL of PBS containing 25% ethanol and incubated in a Shaker at 37 °C with a shaking speed of 100 rpm (Taicang Huada Experimental Instrument Technology Co., Ltd., THZ−C−1, Taicang, China). Secondly, 1 mL of the solution was collected at different time points, and 1 mL of fresh solution was immediately added to maintain the original volume. At last, the collected solution was analysis by UV−Vis spectrophotometer (Thermo Fisher Scientific, Multiskan SkyHigh, Waltham, MA, USA) to evaluate release concentration.

2.5. *Western blot assay*

To study the mechanism by JQI promotes the proliferation of OA and regulates lactic acid. For the Western blot assay, the B16 cells treated with JQ1 of different concentrations were collected and extracted proteins using RIPA lysis buffer containing 1% protease inhibitor, the protein samples extracted from the above cells were separated by SDS-polyacrylamide gel electrophoresis and blotted

onto a nitrocellulose (NC) membrane. The membrane was blocked with 5% BSA for 3 h and incubated with anti-BRD4 antibody (1/1000, *v/v*), anti-phospho-RNA pol II antibody (1/1000, *v/v*), anti-c-Myc antibody (1/1000, *v/v*). anti-HK-2 antibody (1/1000, *v/v*), anti-LDHA antibody (1/1000, *v/v*) or anti-CDK9 antibody (1/1000, *v/v*) at 4 °C overnight. After washing with PBST for three times, the membrane was further incubated with diluted secondary antibody goat anti-rabbit IgG (HRP) (1/5000, *v/v*), then the membrane was washed three times with PBST, and visualized using an ECL reagent with a chemiluminescence system (Thermo Fisher Scientific, iBright CL 1500, Waltham, MA, USA).

2.6. Immunosuppression of lactate on $CD8^+$ T cells

To study the immunosuppressive effect of lactic acid on $CD8^+$ T cells. Firstly, $CD8^+$ T cells were isolated from the spleens of C57BL/6 mice by using a $CD8^+$ notouch isolation kit. $CD8^+$ T cells were seeded into 24-well plates and stimulated with immobilized anti-CD3 mAb (1 μg/mL) and anti-CD28 mAb (1 μg/mL) for 2 days. Secondly, $CD8^+$ T cells were incubated with 0, 10, 20, and 40 mmol/L lactate for 24 h, and the pro-apoptotic effects on $CD8^+$ T cells were evaluated by using the Annexin V/PI apoptosis detection kit according to the manufacturer's instructions. Finally, to evaluate the activity of $CD8^+$ T cells, the same treatment of $CD8^+$ T cells was stained with CD3, CD8 and IFN-γ antibodies. Then, the stained cells were washed with PBS three times and then measured by flow cytometer (BD Bioscience, Aria III, San Jose, CA, USA).

2.7. In vitro immune activation

To verify the *in vitro* activation effect of immune cells, the BMDCs were first extracted from the femur and tibia of C57BL/6 mice and cultured in medium containing 20 ng/mL GM-CSF and 20 ng/mL IL-4 for 7 days. And then, they were seeded into 24-well plates at a density of 5×10^5 cells/well. Secondly, B16 cells were seeded into the upper chamber of transwell plates at a density of 5×10^5 cells/well and treated with different groups, they were co-cultured at 37 °C for 24 h. Finally, BMDCs in the lower chamber were collected, washed twice with PBS and co-stained with anti-CD11c-FITC, anti-CD80-PE, and anti-CD86-APC. The maturation level of BMDCs was then analyzed by flow cytometry. Additionally, the supernatant of the cell culture medium was collected for analyzing the expression levels of cytokines TNF-α and IL-6 by ELISA.

To measure the activation of $CD8^+$ T cells *in vitro*. $CD8^+$ T cells were first isolated from the spleens of C57BL/6 mice by using a $CD8^+$ notouch isolation kit. Then, $CD8^+$ T cells were co-incubated with the aforementioned treated BMDCs for 24 h at a ratio of 1:4 (BMDCs:$CD8^+$ T cells). After that, $CD8^+$ T cells were collected and labeled with anti-CD3, anti-CD8, and anti-IFN-γ antibodies, and analyzed by flow cytometer (BD Bioscience).

2.8. In vivo drug distribution and immune cell recruitment

In order to study the distribution of OA in the tumor tissues. First, the B16 tumor cells (1×10^6 cells) were inoculated on both sides of the mice. Then, the Cy7-labeled OA was administered *via* intratumorally and microneedles, respectively. For *in vivo* imaging, mice were imaged using the *in vivo* imaging system at different time points to evaluate the fluorescence signal distribution in tumors. For *in vitro* detection, mice were euthanized and tumor tissues were dissected at different time points to prepare frozen sections. Briefly, the sections were blocked at room temperature with 5% BSA for 1 h and incubated with anti-Hexon antibody (1/200, *v/v*) at 4 °C overnight. Then, the primary antibody was removed and the sections were incubated with Cy7-labeled secondary antibody at room temperature for 1 h. Finally, the slices were washed three times with PBST and imaged using a slide scanner (Olympus).

For the detection of immune cells in tumor tissues, the mice in each group were euthanized and the tumor tissues were dissected at 48 h. These tissues were further made into frozen sections and blocked at room temperature with 5% BSA for 1 h. Then, incubated with anti-CD4 (1/200, *v/v*), CD8 (1/200, *v/v*), and CD11c (1:200 dilution) antibodies at 4 °C overnight. At last, the slices were washed three times with PBST and imaged by using a slide scanner.

2.9. In vivo immune activation

Female C57 mice (5−6 weeks) were obtained from Beijing Vital River Laboratory Animal Technology Co., Ltd. (Beijing, China). All experimental procedures were executed according to the protocols approved by Beijing Animal Ethics Association and Use Committee of Beijing Institute of Technology (approval ID: 2019-0010- M-152).

To investigate antitumor immune activation *in vivo*, C57BL/6 mice were subcutaneously injected with B16 F10 cells (1×10^6 cells). When the tumor volume reached 100 mm^3, the mice were randomly divided into five groups: PBS, MN-OA, MN-JQ1, i.t.-OJ, and MN-OJ administration. After 48 h, the mice were sacrificed, draining lymph nodes and tumor tissues were collected. Cell suspensions were obtained by filtering through a 70 μm filter. For DCs maturation analysis, cells from DLN were stained with anti-CD11c, CD80, and CD86 antibodies. For CTL analysis, cells from tumors and lymph nodes were stained with anti-CD3, CD8, and IFN-γ antibodies. The stained cells were then washed three times with PBS and measured by flow cytometry (BD Bioscience). The serum in each group was collected for the measurement of lactate, TNF-α, IL-6, IFN-γ, and Granzyme B.

2.10. In vivo antitumor research and biosafety tests

In order to study the anti-tumor effect *in vivo*, a tumor-bearing mouse model was established by subcutaneously injecting 1×10^6 B16 cells into the right side of the mice. When the tumor volume reached 100 mm^3, the mice were randomly divided into the following groups ($n = 6$): PBS, MN-OA, MN-JQ1, i.t.-OJ, MN-OJ. 24 h after inoculation, a distal tumor model was established on the opposite side of the mice, and bilateral tumor growth was measured to assess antitumor efficacy. During the observation period, tumor size and body weight were recorded every other day. The tumor volume was calculated using Eq. (1):

$$\text{Tumor volume} = \text{Length} \times \text{Width} \times \text{Width}/2 \quad (1)$$

where length is longest dimension, width is shortest dimension. At the endpoint of the antitumor study, major organs (heart, liver, spleen, lungs, and kidneys) and tumors were preserved for HE or TUNEL staining to assess the biosafety and apoptosis of tumor cells. Meanwhile, serum obtained from mice to analyze levels of ALT, AST, BUN, and CREA for safety evaluation.

2.11. *Statistical analysis*

Data are presented as the mean ± standard deviation (SD) unless otherwise indicated and were analyzed using GraphPad Prism software version 8 (GraphPad Software Inc., San Diego, CA, USA). The two-tailed unpaired Student's *t*-test was applied to compare the two groups. Statistical significance was indicated as not significant (ns) for $P > 0.05$, $^{*}P < 0.05$, $^{**}P < 0.01$, $^{***}P < 0.001$, and $^{****}P < 0.0001$.

3. Results and discussion

3.1. *JQ1 potentiates OA proliferation and anti-tumor immunity*

To assess the impact of JQ1 on OA proliferation, we measured viral titers after 24 h of treatment with varying JQ1 concentrations. The results showed that JQ1 at 2 μmol/L significantly increased viral infectivity, which was approximately 2.50-fold higher than that with OA alone (Supporting Information Fig. S1). However, at concentrations exceeding 8 μmol/L, viral titers declined, indicating that JQ1 promotes OA proliferation only within a specific concentration range. Therefore, maintaining a stable concentration through continuous release is crucial for the proliferation of OA. Mechanistically, JQ1 induced BRD4−CDK9 complex formation, enhancing CDK9-dependent phosphorylation of RNA Pol II (Fig. 1A and B). Since oncolytic viruses rely on host transcriptional machinery for replication, this phosphorylation facilitates viral gene transcription, elongation, and/or post-transcriptional processing[36,37], thereby boosting OA replication. Consequently, JQ1 at 2 μmol/L enhanced OA proliferation and improved tumor cell killing, as evidenced by increased tumor cell apoptosis in the OA + JQ1 group (Fig. 1C).

The immunosuppressive TME, characterized by PD-L1-mediated T-cell suppression and lactate-induced $CD8^{+}$ T-cell dysfunction, critically contributes to treatment resistance[38,39]. As shown in Fig. 1D and E, JQ1 treatment (>2 μmol/L) effectively suppressed PD-L1 expression on the cell membrane, potentially through direct inhibition of BRD4-mediated PD-L1 transcription[40]. Furthermore, lactate exposure (40 mmol/L) induced severe T-cell exhaustion, evidenced by a 94.7% reduction in IFN-γ secretion (from 33.6% to 1.79%, Fig. 1F and G, Supporting Information Fig. S2) and a 24.4-fold increase in $CD8^{+}$ T-cell apoptosis (from 3.30% to 80.5%, Fig. 1H and I, Supporting

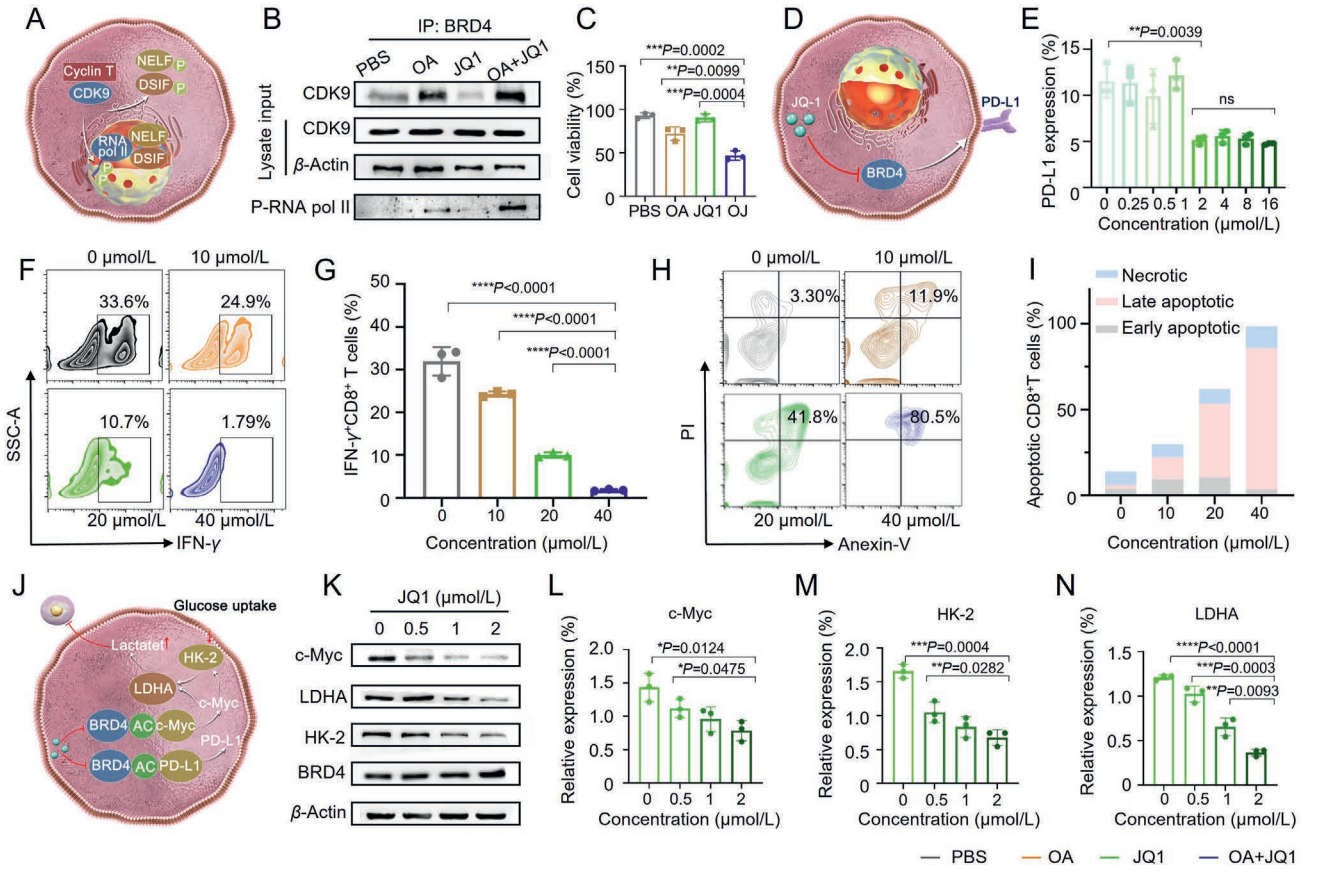

Figure 1 JQ1 potentiates OA efficacy through dual mechanisms of viral potentiation and immune activation. (A) Mechanism of JQ1-mediated enhancement of OA replication. (B) Western blot analysis of BRD4−CDK9 complex formation during OA infection and JQ1 treatment. (C) Cell viability following various treatments. (D) Mechanism of JQ1-mediated PD-L1 suppression. (E) Flow cytometry quantification of PD-L1 expression on B16 cells treated with JQ1 (0−16 μmol/L). (F−I) Flow cytometry analysis and quantification of IFN-$\gamma^{+}CD8^{+}$ T cells (F, G) and apoptotic $CD8^{+}$ T cells (H, I) after 24 h lactate exposure (0−40 mmol/L). (J) Mechanism of JQ1-mediated lactate inhibition. (K−N) Western blot (K) and semi-quantitative analysis of c-Myc (L), HK-2 (M), and LDHA (N) expression following JQ1 treatment. Data are presented as mean ± SD ($n = 3$). Statistically significant differences between groups were identified by unpaired two-tailed Student's *t*-test. $^{****}P < 0.0001$, $^{***}P < 0.001$, $^{**}P < 0.01$, $^{*}P < 0.05$ *vs.* indicated, ns, not significant.

Information Fig. S3). Glycolysis serves as the central energy metabolism pathway in tumor cells, where pyruvate is converted to lactate *via* lactate dehydrogenase (LDHA). Since c-Myc is known to promote glycolysis by upregulating key enzymes LDHA and hexokinase-2 (HK-2) (Fig. 1J)[41], we investigated the potential of JQ1 to modulate lactate production through this regulatory axis. Western blotting analysis revealed that JQ1 significantly reduced the expression of c-Myc in B16 cells in a concentration dependence way (Fig. 1K and L). Furthermore, treatment with 2 μmol/L JQ1 reduced LDHA and HK-2 expression levels by 69.8% and 58.9%, respectively (Fig. 1M and N), demonstrating its ability to suppress lactate accumulation through glycolytic modulation.

Together with its inhibition of PD-L1 expression, the dual action of JQ1, simultaneously blocking immune checkpoint signaling and reducing lactate-mediated immunosuppression, significantly enhances T cell function. These synergistic effects are predicted to amplify the antitumor immune response mediated by OA.

Given the dual ability of JQ1 to potentiate OA replication and augment T-cell-mediated immunity, combined with the intrinsic capacity of OA to induce immunogenic cell death (ICD)[42,43], we hypothesized that their combination would promote dendritic cell (DC) maturation and CTL activation (Fig. 2A). To test this, bone marrow-derived DCs (BMDCs) were co-cultured for 24 h with B16 cells treated with PBS, OA, JQ1, or OA + JQ1. Flow cytometry analysis revealed that the OA + JQ1 combination significantly elevated expression of DC maturation markers CD80, CD86, and MHC-II. Specifically, the CD80 and CD86 expression increased by 28.9% versus PBS and 11.2% versus OA alone (Fig. 2B and C, Supporting Information Fig. S4), and MHC-II expression increased by 43.5% versus PBS and 10.5% versus OA alone (Fig. 2D and E, Supporting Information Fig. S5). The enhanced DC activation led to improved T cell responses. The OA + JQ1 group showed the highest percentage of IFN-γ-producing T cells (28.3% increase versus PBS and 11.0% increase versus OA alone) (Fig. 2F and G, Supporting Information Fig. S6). Moreover, significant increases in IL-6, TNF-α, IFN-γ, and granzyme B secretion by BMDCs and $CD8^+$ T cells were observed (Fig. 2H−K). These findings demonstrate that the OA + JQ1 combination not only exerts direct oncolytic effects but also elicits a potent antitumor immune response, significantly amplifying therapeutic efficacy.

3.2. *Engineering a multistage microneedle platform for coordinated drug delivery*

The multistage MN patch was fabricated by successively casting JQ1/PLGA mixed organic solution and OA/HA mixed aqueous solution into designed molds (Fig. 3A). Optimization studies

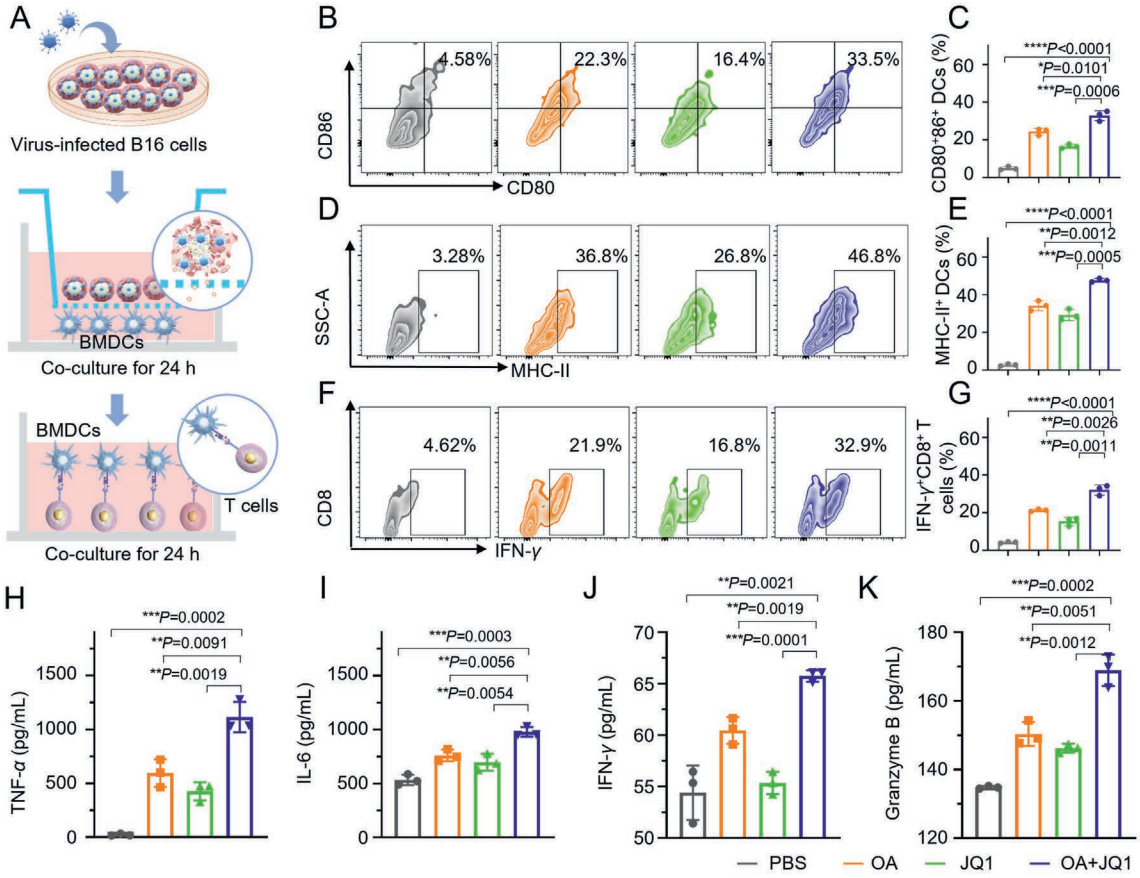

Figure 2 Immune activation by OA and JQ1 combination therapy. (A) Experimental workflow for assessing BMDC and T-cell activation. (B−E) Flow cytometric analysis and quantification of CD80CD86 (B, C) and MHC-II (D, E) expression on BMDCs after 24 h co-culture with different formulations. (F, G) Flow cytometric analysis and quantification of IFN-γ^+CD8^+ T cells after treatment with different formulation-activated BMDCs for another 24 h. (H, I) Release of cytokines TNF-α and IL-6 in BMDCs suspensions. (J, K) IFN-γ and granzyme B are release by activated T cells. Data are presented as mean ± SD ($n = 3$). Statistically significant differences between groups were identified by unpaired two-tailed Student's *t*-test. ****$P < 0.0001$, ***$P < 0.001$, **$P < 0.01$, *$P < 0.05$ *vs*. indicated.

identified a 1:2 height ratio (200 μm tip loaded with JQ1 (loading capacity is 0.199%) and 400 μm base loaded with OA (2.79×10^{10} VPs) as optimal for therapeutic delivery. Optical microscopy and scanning electron microscopy (SEM) revealed a pyramid-shaped structure arranged in a 15 × 15 array (400 μm tip-to-tip spacing) on a 1 × 1 cm patch (Fig. 3B and C). Moreover, the surface appeared smooth and uniform, with no visible features to indicate its underlying multistage architecture. To better characterize the multistage structure of MN, fluorescent dyes, rhodamine B (RhB) and FITC, were incorporated into the tip and base of MN patch, respectively. Fluorescence imaging confirmed a distinct hierarchical structure with robust integration between the tip and base (Fig. 3D). The mechanical properties of microneedles were then characterized. As shown in Fig. 3E and F, the microneedles hardly deform when 1−20 N pressure is applied. Moreover, the mean fracture forces of single needles of MN-OJ were 0.11 N, which far exceeded 0.058 N (the threshold for human skin penetration). The skin penetration efficacy of MN-OJ patch was further validated in mice. Methylene blue (MB, Fig. 3G) and the hematoxylin and eosin (H&E, Fig. 3H) staining confirmed microchannel formation in the skin after MN-OJ treatment. These results collectively established that the MN-OJ patch is a mechanically robust system with effective transdermal delivery capability.

As is well known, HA can be rapidly dissolved in interstitial fluid, whereas PLGA degrades slowly[44] To evaluate the drug delivery performance of the multistage MN patch for potential skin cancer therapy, release kinetics were assessed in PBS containing 25% ethanol at pH 7.5 and 6.5 (Fig. 3I). Upon immersion, the HA needle bases dissolved within minutes (Supporting Information Movie S1), releasing encapsulated FITC in a near-linear manner over 30 min before plateauing (Fig. 3J, Supporting Information

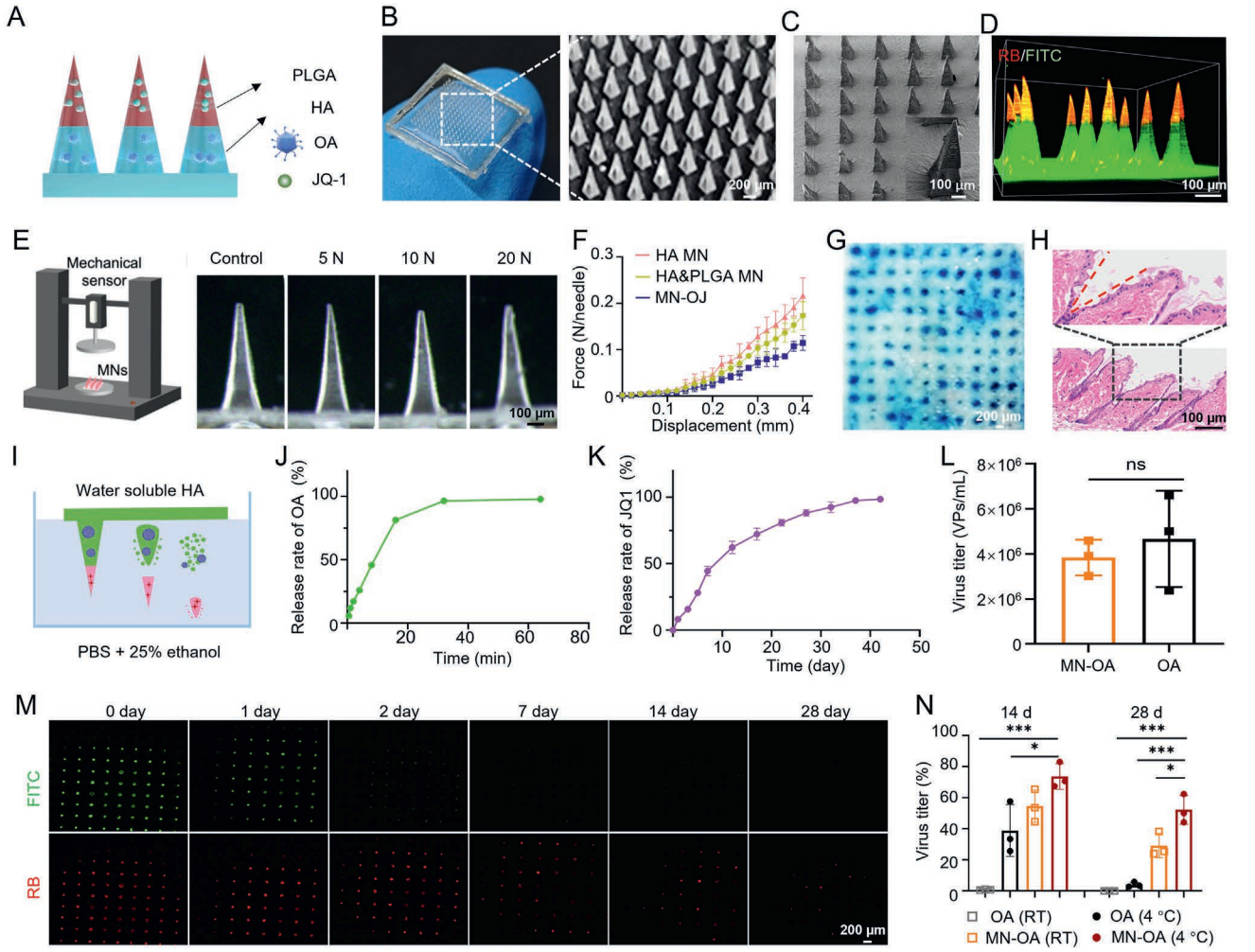

Figure 3 Characterization of the multistage MN patch. (A) Schematic illustration of the multistage MN patch with multi-level structures. (B, C) Typical photograph (B) and SEM image (C) of MN-OJ patch. Scale bar = 100 μm. (D) The fluorescence image of the dye-labeled MN patch (Red: RB, Green: FITC). Scale bar = 100 μm. (E) The deformation under different pressures of MN-OJ patch. Scale bar = 100 μm. (F) Comparison of the mechanical properties of drug-loaded MN (MN-OJ), unloaded multistage MN (PLGA&HA MN), and blank HA patch (HA MN). (G, H) Typical photograph (G) and H&E image (H) of skin section with MN-OJ treatment. Scale bar = 100 μm. (I) Schematic illustration of the drug delivery performance of MN patch. (J, K) The release properties of MN patch *in vitro*. (L) Virus titers of unloaded- or released-OA of MN patch determined by qPCR. (M) *In vivo* release kinetics of MN patch (Red: RB, Green: FITC). Scale bar = 200 μm. (N) Stability of MN-OA patch stored in PBS containing 10% FBS at 4 °C or room temperature (RT) over different time periods. Data are presented as means ± SD ($n = 3$). Statistically significant differences between groups were identified by unpaired two-tailed Student's *t*-test. ***$P < 0.001$, *$P < 0.05$ *vs.* indicated, ns, not significant.

Fig. S7). Following HA dissolution, the PLGA tips remained intact (Movie S1), enabling sustained JQ1 release. Remarkably, JQ1 maintained a steady release rate for over 7 weeks (Fig. 3K). Subsequently, the release kinetics of such MN patch *in vivo* was further evaluated by piercing the above-mentioned dye-labeled multistage MN patches into the tumor tissues of B16 tumor-bearing mice. Time-lapse observations revealed that the FITC signal (HA component) diminished within 24 h in tumors, indicating complete release, while the RhB signal (PLGA component) persisted for 28 days, demonstrating prolonged drug delivery (Fig. 3M). These results confirm the dual-phase release capability of MN patch, solidifying its utility as a robust transdermal delivery platform.

Following dissolution, the infectivity of released OA was quantified using the $TCID_{50}$ assay. The results demonstrated comparable infectivity between MN-released OA and untreated controls (Fig. 3L), confirming full preservation of viral activity after MN encapsulation. Long-term stability studies revealed that the MN-encapsulated OA maintained 52.2% activity after 4 weeks at 4 °C, whereas non-encapsulated OA showed near-complete activity loss. These findings highlight the ability of MN patch to sustain OA infectivity during extended storage (Fig. 3N).

3.3. Spatiotemporally controlled MN-OJ delivery orchestrates antitumor immunity

The excellent penetration ability and controlled drug release properties of the MN-OJ patch, together with the potent immune activation and tumor microenvironment modulation demonstrated by OA + JQ1 combination *in vitro*, prompted us to investigate its performance in B16 tumor-bearing mice. Pharmacokinetic studies using Cy7-labeled OA revealed sustained intratumoral fluorescence for >48 h with MN-OJ delivery, compared to complete clearance within 24 h following conventional intratumoral injection (Fig. 4A and B). Immunohistochemical analysis further

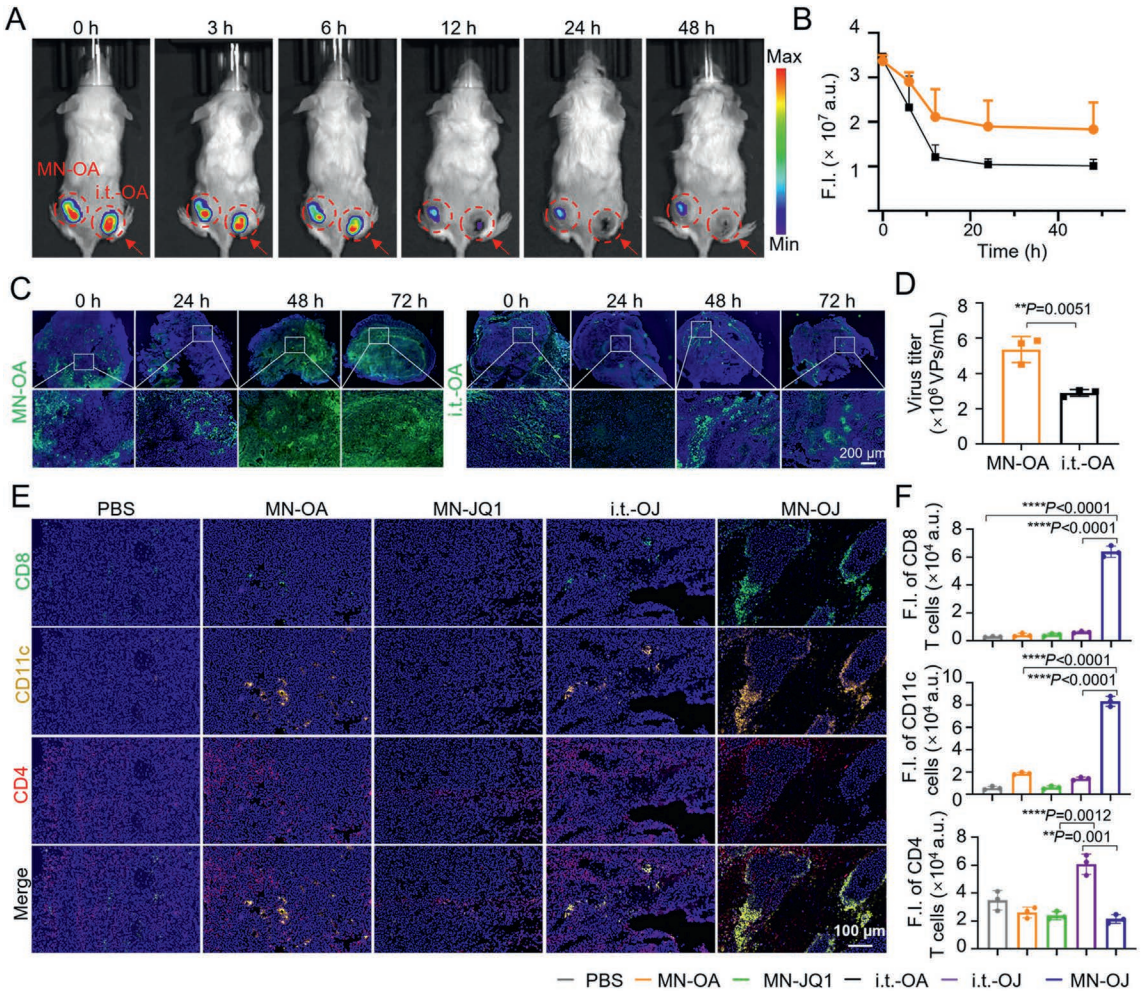

Figure 4 Evaluation of intratumoral drug retention, tissue permeation capabilities of MN-OJ, and immune cell infiltration. (A) *In vivo* fluorescence imaging of Cy7-labeled OA following different administration routes at indicated time points (i.t.-OA (right leg), intratumoral injection of OA, MN-OA (left leg), microneedle injection of OA). (B) Quantitative analysis of relative fluorescence intensity at different time points. (C) Tissue distribution analysis of OA in tumor sections following different administration routes at indicated time points (Green: FITC-conjugated anti-Hexon mAb). Scale bar = 200 μm. (D) Virus titers of OA following different administration routes at 48 h. (E) Fluorescence imaging of tumor-infiltrating DCs (CD11c-PE) and effector T cells (CD4-APC, CD8-FITC) Scale bar = 100 μm. (F) Quantitative analysis of tumor-infiltrating immune cells. PBS: drug-free MN patches; MN-OA: OA-loaded in HA needle base only; MN-JQ1: JQ1-loaded in PLGA needle tips only; i.t.-OJ: intratumoral OA + JQ1 injection; MN-OJ: combinatorial OA (HA base) + JQ1 (PLGA tips) MN system. Data are presented as means ± SD (n = 3). Statistically significant differences between groups were identified by unpaired two-tailed Student's t-test. ****$P < 0.0001$, **$P < 0.01$, *vs.* indicated.

revealed that, compared to conventional intratumoral injection, MN-OA administration significantly improved OA diffusion throughout tumor tissue and promoted sustained OA proliferation over time (Fig. 4C). Furthermore, by using microneedles for drug delivery of JQ1+OA further enhanced the proliferation of OA within the tumor (Supporting Information Fig. S8). Therefore, the virus titers of OA in MN-OA group were almost 2-fold more than that of i.t.-OA group at 48 h post-infection (Fig. 4D). These findings demonstrate the dual advantage of MN-OJ patch superior drug retention and enhanced tissue distribution over standard delivery methods. Additionally, Immunofluorescence analysis of tumor sections showed that MN-OJ treatment significantly increased infiltration of antigen-presenting cells ($CD11c^+$ DCs) and effector T cells ($CD4^+$ and $CD8^+$ T cells) (Fig. 4E). Specifically, the populations of $CD11c^+$ DCs were elevated 4.45-fold (versus MN-OA) and 5.93-fold (versus i.t.-OJ), and the populations of $CD8^+$ T cells were elevated 15.3-fold (*vs*. MN-OA) and 10.3-fold (*vs*. i.t.-OJ), respectively (Fig. 4F). These results demonstrate that the multistage MN-OJ system not only prolongs drug retention but also effectively recruits immune cells to the TME. Together, these findings position the MN-OJ platform as a robust delivery strategy for combined oncolytic virotherapy and immunotherapy.

To further evaluate systemic immune activation *in vivo*, B16 tumor-bearing mice were randomly divided into five groups: (1. PBS group, 2. MN-OA, 3. MN-JQ1, 4. i.t.-OJ, 5. MN-OJ). At 48 h post-administration, we analyzed immune cell activation in draining lymph nodes (DLNs) and tumors by flow cytometry. In the DLNs, the MN-OJ group increased the populations of $CD11c^+CD80^+CD86^+$ DCs by 15.2% and 14.4%, compared to the MN-OA and i.t.-OJ groups, respectively (Fig. 5A and B, Supporting Information Fig. S9). Similarly, the populations of IFN-$\gamma^+CD3^+CD8^+$ T cells were elevated 1.92-fold (*vs*. MN-OA) and 1.56-fold (*vs*. i.t.-OJ) (Fig. 5C and D, Supporting Information Fig. S10). Furthermore, in the tumor tissue, the MN-OJ group also significantly increased the ratio of IFN-$\gamma^+CD3^+CD8^+$ T cells (Fig. 5E and F, Supporting Information Fig. S11). Additionally, we observed an increase in serum levels of cytokines associated with anti-tumor immune responses, including IL-6, TNF-α, IFN-γ, and Granzyme B, further demonstrating the effectiveness of the MN-OJ group in enhancing anti-tumor immune responses (Fig. 5H−K). Mechanistic studies confirmed this effect was

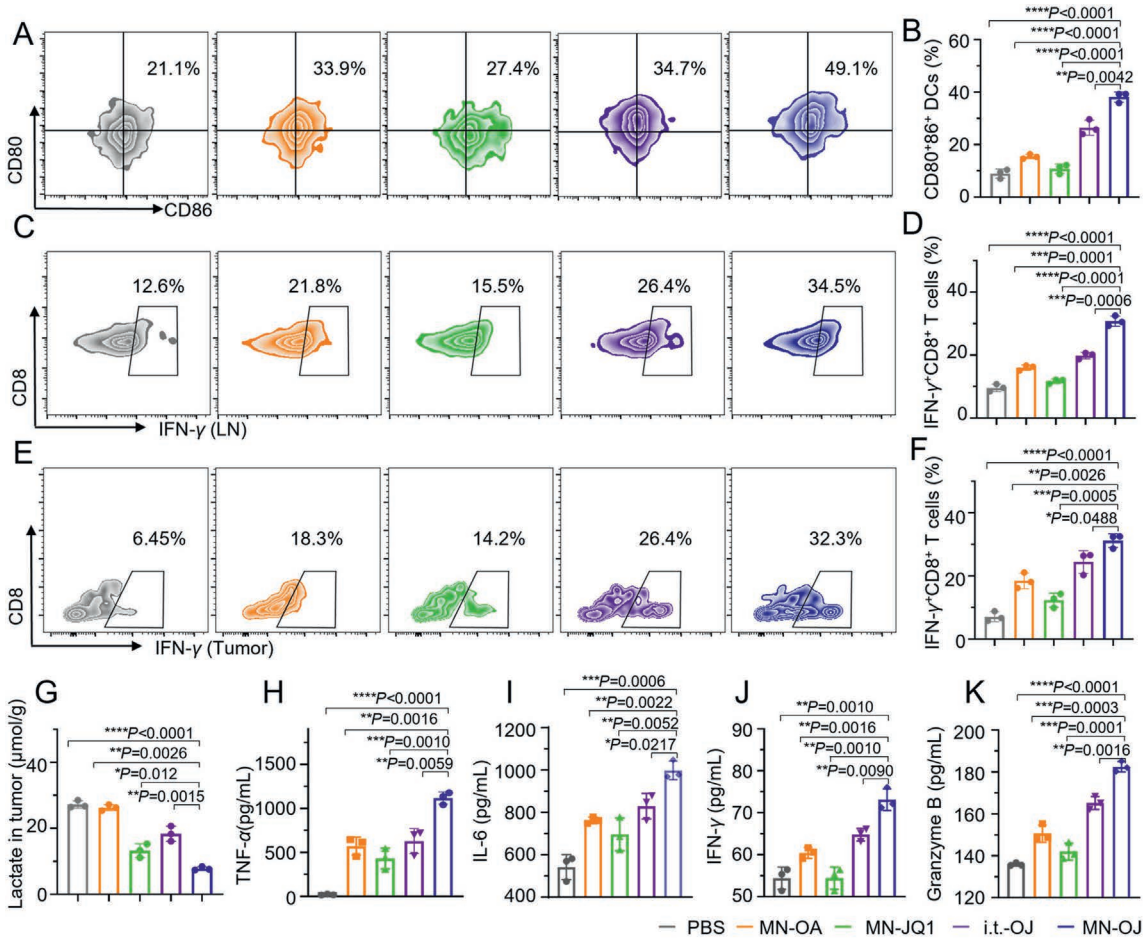

Figure 5 Enhanced systemic immune responses by MN-OJ in B16F10 tumor-bearing mice. (A, B) Flow cytometric analysis and quantification of CD80 and CD86 expression of $CD11c^+$ DCs in LNs on day 2 post-immunization. (C−F) Flow cytometric analysis and quantification of IFN-γ CD8 expression of $CD3^+$ T cells in LNs (C, D) and in tumors (E, F). (G) Intratumoral lactate concentration following treatment across experimental groups. (H−K) Systemic proinflammatory cytokine TNF-α (H), IL-6 (I), IFN-γ (J) and granzyme B (K) levels in serum. Data are presented as means ± SD ($n = 3$). Statistically significant differences between groups were identified by unpaired two-tailed Student's *t*-test. $^{****}P < 0.0001$, $^{***}P < 0.001$, $^{**}P < 0.01$, $^{*}P < 0.05$ *vs*. indicated.

dependent on JQ1-mediated TME remodeling as MN-OJ treatment substantially reduced intratumoral lactate accumulation (Fig. 5G). These results demonstrate that the MN-OJ platform orchestrates proinflammatory cytokine secretion, DC recruitment and maturation, and tumor-specific $CD8^+$ T cell activation *via* OA-induced tumoricidal effects, metabolic reprogramming through JQ1-mediated lactate modulation.

3.4. MN-OJ patch sustains tumor regression and prevents relapse

Encouraged by the immune activation effects, we evaluated the anti-tumor efficacy of MN-OJ *in vivo*. First, a bilateral tumor model was established by successively inoculating B16F10 cells at the right flank (as the primary tumors) and left flank (as the abscopal tumors) of C57BL/6 mice. When the primary tumors reached 100 mm^3, mice were randomly divided into five groups, with primary tumors receiving single-dose MN-OJ or control treatments. Abscopal tumors were inoculated one day after treatment and left untreated (Fig. 6A). The results showed that tumor volumes in both primary and abscopal sites of control groups exhibited negligible suppression (Fig. 6B). The single-drug groups (MN-OA and MN-JQ1) exhibited relatively weak anti-tumor effects, with inhibition rates of 25.9% and 11.37%, respectively. Notably, MN-OJ demonstrated superior therapeutic performance compared to single-drug or mixture formulations, achieving

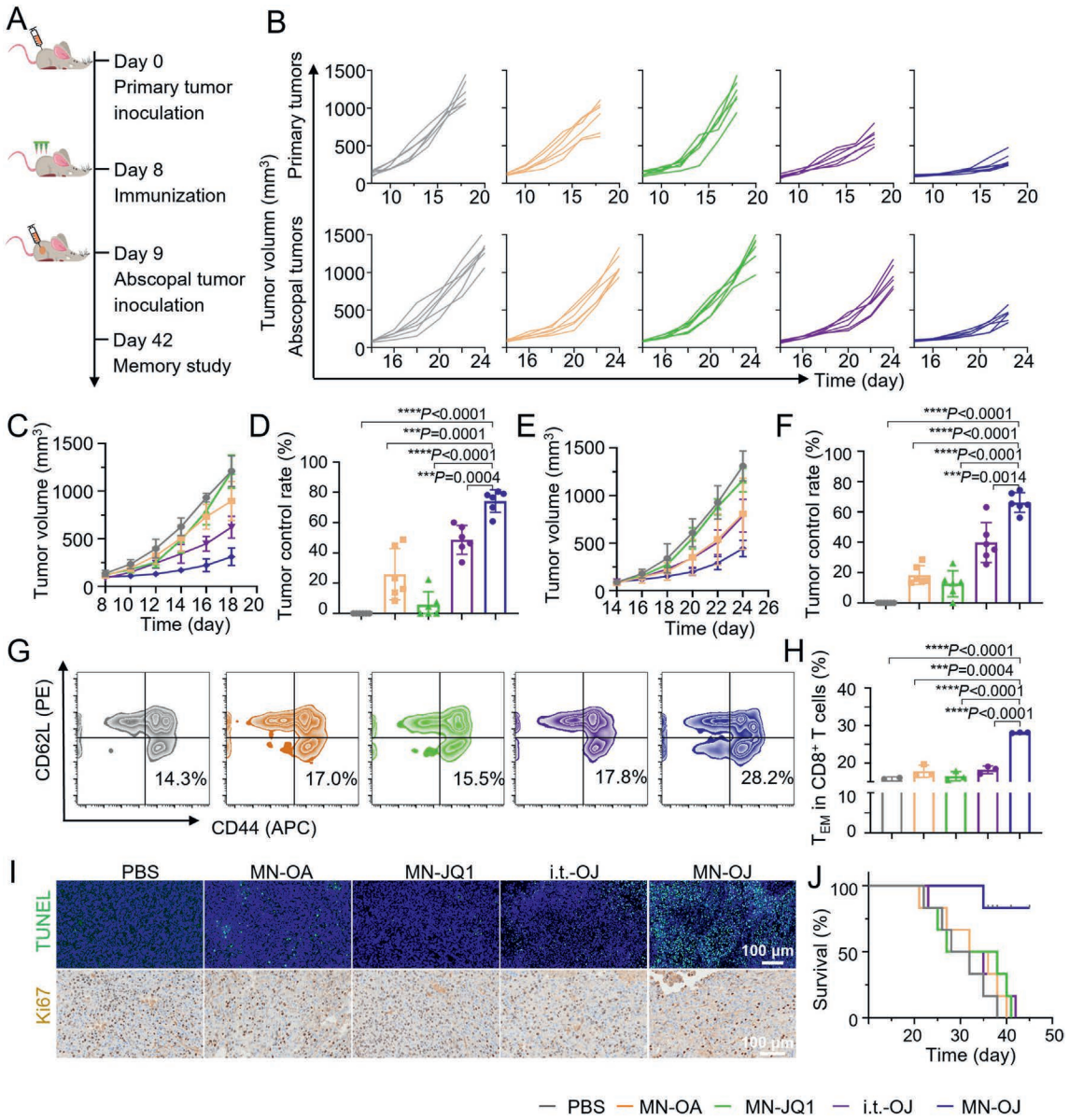

Figure 6 Antitumor effects of MN-OJ against primary and abscopal B16F10 tumors. (A) Schematic illustration of the bilateral tumor model evaluating MN-OJ therapeutic effects. (B) Growth kinetics of primary and distant tumors were measured every 48 h. (C−F) Quantitative analysis of tumor volumes and tumor control rate for primary (C, D) and abscopal (E, F) tumors. (G, H) Flow cytometry data and quantification of $CD3^+CD8^+CD44^+CD62L^-$ T lymphocytes (T_{EM}) in spleens on day 42. (I) TUNEL and Ki67 staining of tumors at the end of the experiment. Scale bar = 100 μm. (J) Survival curves across treatment groups. Data are presented as means ± SD (n = 6). Statistically significant differences between groups were identified by unpaired two-tailed Student's t-test. $^{****}P < 0.0001$, $^{***}P < 0.001$ *vs.* indicated.

74.2% for the primary tumor and 65.4% for the abscopal tumor (Fig. 6C−F).

Long-term memory is essential for preventing tumor recurrence and metastasis. Encouraged by antigen-specific $CD8^+$ CTL-mediated tumor suppression in the above studies, we evaluated the memory response induced in the MN-OJ-treated group. As shown in Fig. 6G and H, Supporting Information Fig. S12**,** compared to the PBS control group, the frequency of effector memory T cells (T_{EM}) ($CD3^+CD8^+CD44^+CD62L^-$) in MN-OJ-treated mice increased by 13.9%, indicating that MN-OJ can induce effective long-term immune memory effects to prevent tumor recurrence. Furthermore, TUNEL staining revealed significantly increased apoptosis in MN-OJ-treated tumors (Fig. 6I), and survival analysis showed 80% survival in the MN-OJ group versus complete mortality in controls within 40 days (Fig. 6J, Supporting Information Fig. S13). Overall, our MN-OJ patch showed significant antitumor effects *in vivo*, effectively killing tumor cells and activating immune responses to suppress tumor growth. Furthermore, MN-OJ treatment induces long-term immune memory effects, providing an abscopal effect that prevents tumor recurrence.

H&E staining of main organs from the treated mice showed that MN-OJ caused no histologically detectable toxicity to normal tissues (Supporting Information Fig. S14). Moreover, biomarkers of hepatic function, including alanine transaminase (ALT), aspartate transaminase (AST), as well as renal function biomarkers, including creatinine (CREA) and urea nitrogen (BUN), were all normal in MN-OJ-treated mice (Supporting Information Fig. S15). These results suggest the satisfactory safety profile of the MN-OJ antitumor therapy.

4. Discussion and conclusions

In summary, we developed a multistage-responsive microneedle (MN-OJ) system for spatiotemporally controlled co-delivery of oncolytic virus OA and the small-molecule inhibitor JQ1 to tumors. This platform integrates material innovation, kinetic precision, and immunomodulatory synergy to address key challenges in oncolytic immunotherapy.

Conventional delivery strategies for oncolytic adenoviruses (intratumoral and intraperitoneal injection) showed limited therapeutic efficacy due to poor targeting precision and uneven intratumoral distribution[45,46]. Intravenous delivery led to rapid viral clearance by neutralizing antibodies and sequestration in non-target organs, while intratumoral injection was hampered by the dense and heterogeneous tumor microenvironment, resulting in suboptimal viral penetration and infection efficiency[47]. Intraperitoneal injection was further restricted to abdominal tumors and complicated by the heterogeneous peritoneal milieu, limiting uniform viral diffusion[48]. Our constructed microneedle MN-OJ significantly enhanced viral accumulation and distribution within tumors while reducing off-target effects. The innovations and advantages of the MN-OJ include (1) minimally invasive and clinically practical delivery. MN-OJ enables pain-free intratumoral delivery of OA, bypassing systemic toxicity while ensuring viral bioactivity during storage/transport-a transformative advantage over intravenous delivery. (2) Precision-engineered therapeutic efficacy. Optimized microneedle design ensures deep tissue penetration, uniform drug distribution, and prolonged intratumoral drug levels (>48 h), enhancing intratumoral bioavailability while minimizing off-target effects. (3) Kinetically distinct drug release. Rapid OA release triggers immediate tumor lysis and ICD. Sustained JQ1 release maintains optimal concentrations to enhance OA replication (2.50-fold increase in viral titers versus controls), thereby enhancing virus-mediated tumoricidal effects. (4) Synergistic immune cascade. The interplay between OA-mediated ICD and JQ1-driven immunosuppressive pathways blockade converts "cold" tumors to "hot" and establishes powerful systemic immunity (abscopal tumor regression in 66.2% of preclinical models) following single-dose treatment.

The system leverages FDA-approved materials (PLGA, HA) and clinically validated agents (OA, JQ1), accelerating translational potential. Its modular design adapts to tumor size/depth through adjustable MN length, MN sizes. However, challenges remain: current studies are limited to preclinical models, and validation in patient-derived organoids or PDX models is needed to refine clinical applicability. Future integration with stimuli-responsive nanomaterials (*e.g.*, light-, thermal-, or magnetic-responsive agents) could enable real-time imaging and precision-controlled combination therapies.

By harmonizing localized oncolysis with systemic immune activation, this MN-OJ platform represents a versatile strategy for spatiotemporally coordinated cancer immunotherapy. Its clinical feasibility, combined with potential for personalized adaptation, positions it as a promising candidate for translational development.

Acknowledgements

We thank Shanghai Yuansong Biotechnology Co., Ltd. for providing OA (ZD55-IL24). This work was funded by the National Natural Science Foundation of China (22274011), Hebei Natural Science Foundation (B2024105013), Beijing Natural Science Foundation-Haidian Original Innovation Joint Program (L242138), Beijing Chen Jumei Public Welfare Foundation (202524141003A), Henan Province Science and Technology Research Project (252102310424), Innovative Drug Research and Development—National Science and Technology Major Project (2025ZD1801600), Capital's Funds for Health Improvement and Research (CFH 2024-1-4052) and National Health Commission Clinical Research Projects for Innovative Drugs (WKZX2023CX210007).

Author contributions

Zhongjie Wang designed the research. Zhongjie Wang and Zewei Yan carried out the experiments and performed data analysis. Hanlin Chen and Shujun Liu participated part of the experiments. Yue Wang Yuantian Jing and Yingjie Shi provided experimental drugs and quality control. Lili Huang wrote the manuscript. Guanghao Wu and Pengfei Jin revised the manuscript. All of the authors have read and approved the final manuscript.

Conflicts of interest

The authors declare no conflicts of interest.

Supporting information

Supporting information to this article can be found online at https://doi.org/10.1016/j.apsb.2026.02.015.

References

1. Mathlouthi S, Kuryk L, Prygiel M, Lupo MG, Zasada AA, Pesce C, et al. Extracellular vesicles powered cancer immunotherapy: targeted delivery of adenovirus-based cancer vaccine in humanized melanoma model. *J Control Release* 2024;**376**:777−93.
2. Zhao A, Zhou C, Li J, Wang Z, Zhu H, Shen S, et al. UBE2G2 inhibits vasculogenic mimicry and metastasis of uveal melanoma by promoting ubiquitination of LGALS3BP. *Acta Pharm Sin B* 2024;**14**: 5201−18.
3. von Schuckmann LA, Hughes MCB, Ghiasvand R, Malt M, van der Pols JC, Beesley VL, et al. Risk of melanoma recurrence after diagnosis of a high-risk primary tumor. *JAMA Dermatol* 2019;**155**: 688−93.
4. Robertson BM, Fane ME, Weeraratna AT, Rebecca VW. Determinants of resistance and response to melanoma therapy. *Nat Cancer* 2024;**5**: 964−82.
5. Centeno PP, Pavet V, Marais R. The journey from melanocytes to melanoma. *Nat Rev Cancer* 2023;**23**:372−90.
6. Szadai L, Guedes JS, Woldmar N, de Almeida NP, Jánosi ÁJ, Rajeh A, et al. Mitochondrial and immune response dysregulation in melanoma recurrence. *Clin Transl Med* 2023;**13**:e1495.
7. Liu H, Ou J, Hung MC, Chen X. Immune checkpoint blockades therapy of melanoma. *Sci Bull* 2023;**68**:356−8.
8. Telarovic I, Yong CSM, Kurz L, Vetrugno I, Reichl S, Fernandez AS, et al. Delayed tumor-draining lymph node irradiation preserves the efficacy of combined radiotherapy and immune checkpoint blockade in models of metastatic disease. *Nat Commun* 2024;**15**:5500.
9. Otto G. Diverse routes to melanoma metastasis and ICI resistance. *Nat Cancer* 2023;**4**:1643.
10. Huang AC, Zappasodi R. A decade of checkpoint blockade immunotherapy in melanoma: understanding the molecular basis for immune sensitivity and resistance. *Nat Immunol* 2022;**23**:660−70.
11. Franklin C, Mohr P, Bluhm L, Grimmelmann I, Gutzmer R, Meier F, et al. Impact of radiotherapy and sequencing of systemic therapy on survival outcomes in melanoma patients with previously untreated brain metastasis: a multicenter DeCOG study on 450 patients from the prospective skin cancer registry ADOREG. *J Immunother Cancer* 2022;**10**:e004509.
12. Zhao M, Xu R, Yang Y, Tong L, Liang J, Jiang Q, et al. Bioabsorbable nano-micelle hybridized hydrogel scaffold prevents postoperative melanoma recurrence. *J Control Release* 2023;**356**:219−31.
13. Kanaya N, Kitamura Y, Lopez Vazquez M, Franco A, Chen KS, van Schaik TA, et al. Gene-edited and -engineered stem cell platform drives immunotherapy for brain metastatic melanomas. *Sci Transl Med* 2023;**15**:eade8732.
14. Liu J, Wang X, Li Z, Gao S, Mao L, Dai J, et al. Neoadjuvant oncolytic virus orienx010 and toripalimab in resectable acral melanoma: a phase Ib trial. *Signal Transduct Target Ther* 2024;**9**:318.
15. Lee WS, Lee SJ, Lee HJ, Yang H, Go EJ, Gansukh E, et al. Oral reovirus reshapes the gut microbiome and enhances antitumor immunity in colon cancer. *Nat Commun* 2024;**15**:9092.
16. Lin J, Sun S, Zhao K, Gao F, Wang R, Li Q, et al. Oncolytic parapoxvirus induces gasdermin E-mediated pyroptosis and activates antitumor immunity. *Nat Commun* 2023;**14**:224.
17. Wu Q, Huang H, Sun M, Zhang R, Wang J, Zheng H, et al. Inhibition of ttumor metastasis by liquid-nitrogen-shocked tumor cells with oncolytic viruses infection. *Adv Mater* 2023;**35**:e2212210.
18. Gujar S, Bell J, Diallo JS. SnapShot: cancer immunotherapy with oncolytic viruses. *Cell* 2019;**176**:1240.
19. Poh A. First oncolytic viral therapy for melanoma. *Cancer Discov* 2016;**6**:6.
20. Wan PK, Fernandes RA, Seymour LW. Oncolytic viruses and antibodies: are they more successful when delivered separately or when engineered as a single agent?. *J Immunother Cancer* 2023;**11**:e006518.
21. Elzoghby AO, Samir O, Emam HE, Soliman A, Abdelgalil RM, Elmorshedy YM, et al. Engineering nanomedicines for immunogenic eradication of cancer cells: recent trends and synergistic approaches. *Acta Pharm Sin B* 2024;**14**:2475−504.
22. Lin D, Shen Y, Liang T. Oncolytic virotherapy: basic principles, recent advances and future directions. *Signal Transduct Target Ther* 2023;**8**: 156.
23. Liu S, Li F, Ma Q, Du M, Wang H, Zhu Y, et al. OX40L-armed oncolytic virus boosts T-cell response and remodels tumor microenvironment for pancreatic cancer treatment. *Theranostics* 2023;**13**:4016−29.
24. Wang Y, Zhou Y, Yang L, Lei L, He B, Cao J, et al. Challenges coexist with opportunities: spatial heterogeneity expression of PD-L1 in cancer therapy. *Adv Sci* 2024;**11**:e2303175.
25. Certo M, Tsai CH, Pucino V, Ho PC, Mauro C. Lactate modulation of immune responses in inflammatory versus tumour microenvironments. *Nat Rev Immunol* 2021;**21**:151−61.
26. Zhang Z, Zhou Y, Zhao S, Ding L, Chen B, Chen Y. Nanomedicine-enabled/augmented cell pyroptosis for efficient tumor nanotherapy. *Adv Sci* 2022;**9**:e2203583.
27. Feng M, Xu H, Zhou W, Pan Y. The BRD4 inhibitor JQ1 augments the antitumor efficacy of abemaciclib in preclinical models of gastric carcinoma. *J Exp Clin Cancer Res* 2023;**42**:44.
28. Zhou M, Wang J, Pan J, Wang H, Huang L, Hou B, et al. Nanovesicles loaded with a TGF-β receptor 1 inhibitor overcome immune resistance to potentiate cancer immunotherapy. *Nat Commun* 2023;**14**:3593.
29. Zhang Y, Yu R, Zhao C, Liang J, Zhang Y, Su H, et al. CAFs homologous biomimetic liposome bearing BET inhibitor and pirfenidone synergistically promoting antitumor efficacy in pancreatic ductal adenocarcinoma. *Adv Sci* 2024;**11**:e2305279.
30. Leal AS, Williams CR, Royce DB, Pioli PA, Sporn MB, Liby KT. Bromodomain inhibitors, JQ1 and I-BET 762, as potential therapies for pancreatic cancer. *Cancer Lett* 2017;**394**:76−87.
31. Zhang H, Lu L, Yi C, Jiang T, Lu Y, Yang X, et al. BRD4 regulates m^6A of ESPL1 mRNA *via* interaction with ALKBH5 to modulate breast cancer progression. *Acta Pharm Sin B* 2025;**15**:1552−70.
32. Ding J, Lu Y, Zhao X, Long S, Du J, Sun W, et al. Activating iterative revolutions of the cancer-immunity cycle in hypoxic tumors with a smart nano-regulator. *Adv Mater* 2024;**36**:e2400196.
33. Zhu W, Zhou Z, Yang M, Chen X, Zhu S, Yu M, et al. Injectable nanocomposite immune hydrogel dressings: prevention of tumor recurrence and anti-infection after melanoma resection. *Small* 2024; **20**:e2309476.
34. Peng T, He Y, Shao X, Liu H, Yang L, Xiong W, et al. Reversing tumor fibrosis for potentiating chemo-immunotherapy *via* lactic acid exhaustion by codelivery of bicarbonate and JQ1. *Nano Today* 2025; **61**:102657.
35. Ding L, Guo H, Zhang J, Zheng M, Zhang W, Wang L, et al. Zosuquidar promotes antitumor immunity by inducing autophagic degradation of PD-L1. *Adv Sci* 2024;**11**:2400340.
36. Wang S, Liang B, Wang W, Li L, Feng N, Zhao Y, et al. Viral vectored vaccines: design, development, preventive and therapeutic applications in human diseases. *Signal Transduct Target Ther* 2023;**8**:149.
37. Shen Y, Bai X, Zhang Q, Liang X, Jin X, Zhao Z, et al. Oncolytic virus VG161 in refractory hepatocellular carcinoma. *Nature* 2025;**641**: 503−11.
38. Wang X, Lu L, Hong X, Wu L, Yang C, Wang Y, et al. Cell-intrinsic PD-L1 ablation sustains effector $CD8^+$ T cell responses and promotes antitumor T cell therapy. *Cell Rep* 2024;**43**:113712.
39. Peralta RM, Xie B, Lontos K, Nieves-Rosado H, Spahr K, Joshi S, et al. Dysfunction of exhausted T cells is enforced by MCT11-mediated lactate metabolism. *Nat Immunol* 2024;**25**:2297−307.
40. Liang S, Liu M, Mu W, Gao T, Gao S, Fu S, et al. Nano-regulator inhibits tumor immune escape *via* the "two-way regulation" epigenetic therapy strategy. *Adv Sci* 2024;**11**:e2305275.
41. Kumar R, Mishra A, Gautam P, Feroz Z, Vijayaraghavalu S, Likos EM, et al. Metabolic pathways, enzymes, and metabolites: opportunities in cancer therapy. *Cancers* 2022;**14**:5268.
42. Lowenstein PR, Varela ML, Castro MG. The discrete charm of oncolytic viruses: toward the finish line. *Cancer Cell* 2025;**43**:611−8.

43. Lv B, Li J, Li M, Zhuo Y, Ren K, Li E, et al. Enhancement of adenovirus infection and adenoviral vector-mediated gene delivery by bromodomain inhibitor JQ1. *Sci Rep* 2018;**8**:11554.
44. Xiang Y, Lu J, Mao C, Zhu Y, Wang C, Wu J, et al. Ultrasound-triggered interfacial engineering-based microneedle for bacterial infection acne treatment. *Sci Adv* 2023;**10**:eadf0854.
45. Shalhout SZ, Miller DM, Emerick KS, Kaufman HL. Therapy with oncolytic viruses: progress and challenges. *Nat Rev Clin Oncol* 2023; **20**:160−77.
46. Melero I, Castanon E, Alvarez M, Champiat S, Marabelle A. Intratumoural administration and tumour tissue targeting of cancer immunotherapies. *Nat Rev Clin Oncol* 2021;**18**:558−76.
47. Zhong L, Gan L, Wang B, Wu T, Yao F, Gong W, et al. Hyperacute rejection-engineered oncolytic virus for interventional clinical trial in refractory cancer patients. *Cell* 2025;**188**:1119−36.
48. Zhang Y, Qian L, Chen K, Gu S, Meng Z, Wang J, et al. Oncolytic adenovirus in treating malignant ascites: a phase II trial and longitudinal single-cell study. *Mol Ther* 2024;**32**:2000−20.